

# Electrically switchable photonic diode empowered by chiral resonance

Jiaqi Zhao,<sup>1,\*</sup> Kexun Wu,<sup>1,\*</sup> Xuecheng Yan,<sup>1</sup> Jiewen Li,<sup>1</sup> Xiaochuan Xu,<sup>1</sup> Ke Xu,<sup>1</sup> Yu Li,<sup>2</sup> Linjie Zhou,<sup>2</sup> Yan Chen,<sup>3,†</sup> and Jiawei Wang<sup>1,‡</sup>

<sup>1</sup>*School of Integrated Circuits, Harbin Institute of Technology (Shenzhen), Shenzhen, 518055, China*

<sup>2</sup>*State Key Laboratory of Photonics and Communications,  
School of Information Science and Electronic Engineering,  
Shanghai Jiao Tong University, Shanghai, 200240, China*

<sup>3</sup>*Institute for Quantum Science and Technology, National University of Defense Technology, Changsha, 410073, China*

(Dated: August 26, 2025)

The on-chip integration of nonreciprocal optical devices remains a critical challenge for modern optoelectronics, as conventional magneto-optic approaches suffer from material incompatibility and excessive optical losses. Nonlinear photonic diodes have emerged as a promising magnet-free alternative, yet their widespread adoption has been constrained by inherent limitations in reconfigurability. Here, we present an all-silicon, electrically tunable photonic diode leveraging engineered chiral resonances in an ultra-compact microring architecture. The pronounced asymmetric modal coupling enables nonreciprocal transmission with two distinct operation modes at threshold powers down to  $-5$  dBm. The chirality further enables unprecedented control over self-pulsation dynamics, manifesting in propagation-direction-dependent oscillation thresholds and temporal signatures. Crucially, post-fabrication electrical reconfigurability allows dynamic switching between forward, backward, and disabled states. This work represents a significant advancement in integrated nonreciprocal photonics, offering a CMOS-compatible solution with transformative potential for optical interconnects, photonic neural networks, and signal processing systems.

Nonreciprocal optical devices are fundamental components of modern optical systems across classical and quantum domains [1–3]. While commercial devices predominantly rely on magneto-optic (MO) effects [4], their monolithic integration remains challenging due to bulky magnets and material incompatibility with the standard CMOS processes [5–7]. This limitation has spurred extensive research into magnetic-free alternatives, including spatiotemporal index modulation [8, 9] mimicking the MO effect, as well as others circumventing Lorentz reciprocity, e.g., optomechanical [10, 11], optoacoustic [12, 13], and nonlinear optical systems [14–18]. Among these, nonlinearity-based approaches exploit structural and coupling asymmetries to achieve nonreciprocal transmission [14, 19, 20]. Despite the inherent constraints imposed by dynamic reciprocity [21], the approach offers great promise for compact, integrated photonic diodes, capable of temporally separated forward/backward excitations [22], making them especially valuable for shaping and routing of optical signals in densely integrated systems for optical interconnects [23], detection [24], and computing [14, 25].

Recent advances in chiral optical states within non-Hermitian systems have unlocked novel opportunities for manipulating light flow in photonic integrated circuits (PICs) [26]. In particular, engineered chirality in whispering gallery mode resonators has led to remarkable phenomena, including asymmetric backscattering [27], unidirectional emission [28], asymmetric mode switching [29], chiral perfect absorption [30], chiral light-matter interaction [31], as well as non-reciprocal transmission [15]. Unlike the widely investigated Fano-resonance-based photonic diodes [14, 24, 32, 33], chiral resonances provide a compelling alternative with on-demand non-

reciprocal bandwidth and substantially reduced insertion loss. However, existing implementations remain constrained by their reliance on static chiral states [23, 34, 35], relying solely on the passive nonlinearities ( $\chi^{(2)}$  or  $\chi^{(3)}$ ). The inability of electrical reconfigurability in these photonic diodes represents a key barrier to achieving dynamic control over nonreciprocal bandwidth, threshold power, and temporal response characteristics.

In this article, we propose and experimentally demonstrate an electrically tunable photonic diode on a silicon-on-insulator (SOI) platform that harnesses chiral resonances in a compact microring resonator. Owing to unbalanced backscattering induced by spiral-shaped deformations on the microresonators, the mode chirality lifts the contrast in intracavity power between the two excitation directions, turning on the photonic diode with non-reciprocal transmission at a threshold power down to  $-5$  dBm. The photonic diode operates in two distinct modes, differentiated by thermal pre-activation conditions, each exhibiting unique spectral characteristics. Besides, the chirality further governs dynamics of self-pulsation (SP), producing direction-dependent activation thresholds and waveform characteristics. Most significantly, the post-fabrication phase tuning permits full electrical reconfiguration between forward, backward, and disabled states through sign reversal of chirality. The synergistic combination of electrical reconfiguration and operation-dependent nonlinear response represents a fundamental advance over conventional static nonreciprocal devices.

## RESULTS

### WORKING PRINCIPLE

In conventional microring resonators, optical modes exist as degenerate clockwise (CW) and counterclockwise (CCW) traveling waves (see Methods). Chirality emerges through controlled breaking of this degeneracy, typically achieved via either patterned local scatterers [36, 37], or additional mode conversion units [35, 38, 39]. Here our photonic diode employs a compact, holistic design using a microring with spiral-shaped deformation, combined with integrated phase shifter (Fig. 1a). The azimuthal angle  $\theta$ , quantifying the angular spacing between the inner and outer spiral edge, serves as an effective geometric parameter that determines two backscattering terms, namely  $\mathbf{A}$  (CW  $\rightarrow$  CCW) and  $\mathbf{B}$  (CCW  $\rightarrow$  CW) [23, 40] (Supplementary Note 1). By varying  $\theta$ , the mode chirality  $\alpha = (|\mathbf{A}| - |\mathbf{B}|) / (|\mathbf{A}| + |\mathbf{B}|)$  gets efficiently modulated between two extremum cases (see Fig. 1b), ideally two exceptional points (EPs), namely EP+ ( $\mathbf{B} = 0, \alpha = -1$ ) and EP- ( $\mathbf{A} = 0, \alpha = 1$ ), where the system's eigenvalues and associated eigenstates coalesce [41, 42].

At high optical powers, silicon's nonlinear response manifests mainly through the two-photon absorption (TPA) and the free-carrier absorption (FCA). TPA creates free carriers while simultaneously introducing heat into the mode volume, while the free-carrier dispersion (FCD) and thermo-optic (TO) effects induce counteracting resonance shifts (Supplementary Note 2). Overall, the thermal contribution dominates, producing a characteristic redshifted and broadened resonance [43]. Fig. 1c presents the resulting asymmetric lineshape where transmission abruptly recovers as heating saturates and the resonance returns to its initial wavelength [43]. The chiral resonance fundamentally alters these nonlinear dynamics for this waveguide-coupled injection from opposite sides (i.e., ports 1 and 2 in Fig. 1a). For identical injection power  $P_{\text{in}}$ , asymmetric backscattering creates a strong contrast of the intracavity power,  $P_1$  and  $P_2$  (see Fig. 1a), leading to direction-dependent spectral responses. As revealed in the top panel of Fig. 1d, a negative chirality ( $\alpha < 0$  and  $|\mathbf{A}| \ll |\mathbf{B}|$ ) creates a nonreciprocal window (the shaded area), establishing the forward state with blocking of backward transmission.

The photonic diode's functionality can be dramatically enhanced through active control of chirality. Beyond the fixed geometric parameter  $\theta$ , the phase shifter enables adjustment of backscattering strengths via electrical modulation of effective refractive index change  $\Delta n_{\text{eff}}$  (Fig. 1b) [40]. When chirality is reversed ( $\alpha > 0$  and  $|\mathbf{A}| \gg |\mathbf{B}|$ ), the diode switches to backward state (the bottom panel of Fig. 1d). By adjusting  $\alpha$  close to near-zero values, the equalized  $P_1$  and  $P_2$  effectively deactivating the diode through balanced absorption-induced broadening (see Fig. 1e). While both the chirality and the increased input power generally enhance bandwidth through enhanced nonlinear effects, we emphasize that the nonlinear

scaling of the nonreciprocal bandwidth  $\Delta\lambda_{\text{NR}}$  is strongly dependent on the specific operation mode — a relationship we will examine quantitatively in subsequent analysis.

### NON-RECIPROCALITY IN TWO OPERATIONAL MODES

For experimental demonstrations, spiral ring resonators were fabricated on an SOI platform through a foundry service (Fig. 2a and Methods). As shown in Fig. 2b, the transmission spectra ( $T_1$  and  $T_2$ ) were characterized upon reversed excitation direction (Supplementary Note 3 and Methods). For the linear regime, the transmission dips revealing Lorentzian lineshapes, with a loaded Q factor of  $\sim 11300$ , confirm the maintenance of Lorentz reciprocity. Meanwhile, the backreflection spectra  $R_1$  and  $R_2$  revealed pronounced asymmetric scattering with a contrast  $\Delta\Gamma_{\text{BR}}$  of  $\sim 13.5$  dB at the resonance. According to temporal coupled-mode theory (TCMT), mode chirality can be extracted directly based on the reflection signals, i.e.,  $\alpha = \frac{\sqrt{R_1} - \sqrt{R_2}}{\sqrt{R_1} + \sqrt{R_2}}$  [27]. The value of  $\sim -0.6$  suggests a nice agreement with spectral fits of non-Hermitian parameters (Supplementary Note 1).

The photonic diode exhibits two distinct operational modes for nonreciprocal transmission. The first, termed the “pre-activated” mode, employs continuous laser wavelength up-scanning that progressively heats the cavity, resulting in tracing of the “high-temperature state” due to the thermal accumulation and a preserved resonance in the bistable regime (see Fig. 2c-d). This process continues until reaching maximum temperature  $T_{\text{max}}$ , where heat accumulation saturates. The second, which we call the “independent” mode, employs a predefined fixed-wavelength excitation of a cold resonator. While avoiding cumulative heat accumulation, the system reaches a transient critical temperature  $T_{\text{critical}}$  before entering the bistable regime, before returning to its initial temperature  $T_0$  along the low-temperature state trajectory (Supplementary Note 4). Experimental characterization of the transmission spectrum  $Tr_2$  in Fig. 2d reveals that the preactivated mode follows the lower hysteresis trace, while the independent mode follows the upper hysteresis trace.

Power-dependent characterization reveals striking differences between operational modes (Fig. 2e-f). In the pre-activated mode (Fig. 2e), asymmetric lineshapes for both injection directions emerge upon  $P_{\text{in}}$  beyond  $-7$  dBm. Backward injection generates larger resonance redshifts compared to forward injection, reaching a maximum  $\Gamma_{\text{ISO}}$  of 18 dB at  $P_{\text{in}}$  of  $-3$  dBm, before degradation due to enhanced nonlinear absorption effects. The nonreciprocal bandwidth showed continuous expansion with increasing  $P_{\text{in}}$ . The nonreciprocal bandwidth expands continuously to  $\sim 2.9$  nm at 9 dBm, the upper limit of our characterization system (Supplementary Note 5). Notably, backreflection measurements confirm these ef-

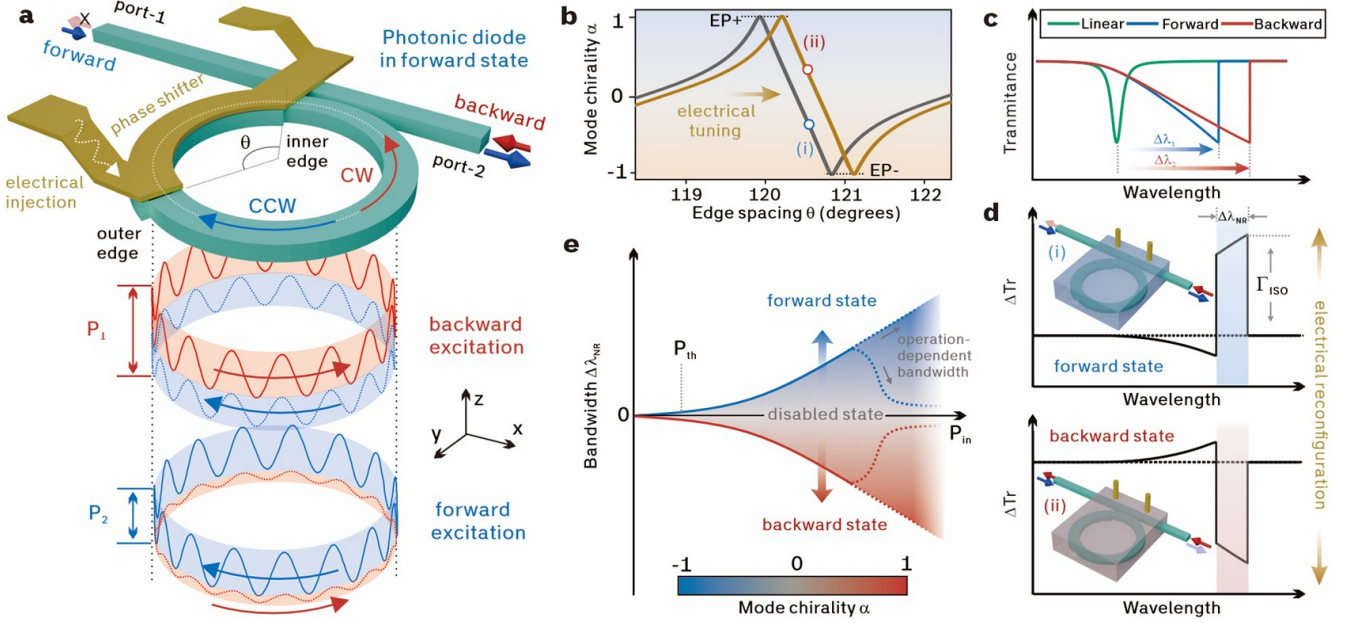


FIG. 1. **Nonreciprocity in a chirality-enabled photonic diode.** **a**, Schematic of a waveguide-coupled spiral ring on an SOI platform operating as an integrated photonic diode in the forward state ( $\alpha < 0$ ), in which backward transmission is prohibited. The integrated thermo-optic phase shifter enables electrical control of mode chirality. **b**, Numerically calculated mode chirality  $\alpha$  as a function of  $\theta$  without (black) and with (brown) electrical tuning. **c**, Schematic of transmission responses in the linear and nonlinear regimes. The isolation ratio  $\Gamma_{\text{ISO}}$  is defined as the highest achievable transmission contrast within the nonreciprocal band. **d**, Transmission contrast  $\Delta Tr = Tr_1 - Tr_2$  as a function of wavelength, with highlighted reconfigurable nonreciprocal band (shaded areas) in the forward (top) and backward (bottom) states. **e**, Schematic showing the evolution of the nonreciprocal bandwidth  $\Delta\lambda_{\text{NR}}$  on the injection power  $P_{\text{in}}$  upon tailorable mode chirality, in which three different operational states are denoted. The threshold power  $P_{\text{th}}$  is defined as the required injection power to achieve  $\Gamma_{\text{ISO}}$  of 3 dB.

fects (Supplementary Note 6). The backreflection within the nonreciprocal band upon forward injection becomes much suppressed down to the noise level, which is close to the ideal scenario of nearly reflectionless transmission without any resonance-induced perturbation.

For the independent mode (Fig. 2f), the asymmetric lineshapes emerge at a comparable power level ( $P_{\text{in}} \sim -5$  dBm), and the nonreciprocal transmission reaches  $\Gamma_{\text{ISO}}$  of  $\sim 13$  dB upon further lifted  $P_{\text{in}}$ . Notably, the nonreciprocal bandwidth saturates at  $P_{\text{in}} \sim -4$  dBm. This distinction stems from the limit of resonance redshift that remains constrained within the cold resonant regime (see Fig. 2g, and Supplementary Note 4). Despite the limited bandwidth, this configuration-free operation represents a crucial “plug-and-play” functionality, absent in previous photonic diode studies but essential for practical applications.

### CHIRALITY-MEDIATED SELF-PULSATION

The engineered chiral resonance gives rise to unprecedented control of complex time-domain dynamics under even a continuous-wave excitation. In experiments at high  $P_{\text{in}}$  (Fig. 3a–b), the original equilibrium state becomes unstable through a Hopf bifurcation, subsequently being re-stabilized as self-sustained pulse se-

quences with frequency  $\omega_{\text{SP}}$  around 1–2 MHz. The chiral produces markedly different SP dynamics for opposite injections. Forward injection requires higher activation power ( $P_{\text{SP2}} \approx 0$  dBm) to initiate SP compared to backward propagation ( $P_{\text{SP1}} \approx -2$  dBm), which is a direct consequence of the chirality-induced intracavity power imbalance ( $P_2 < P_1$ ). The SP phenomena evolve dramatically with increasing  $P_{\text{in}}$ , with the oscillation band expanding within the thermally broadened resonance while maintaining distinct directional characteristics. Forward injection maintains a moderate bandwidth compared to the backward injection, with nearly reflectionless and lossless transmission outside the SP band.

Fig. 3c presents two characteristic cases of SP waveforms. Near the threshold (case i, left panel), each oscillation period initiates with a transmission dip ( $\sim 0.1 \mu\text{s}$  duration), followed by a slow decay. For high-power operation (case ii, right panel), the oscillating waveform reveals a  $\sim 15$  ns transient pulse as a clear signature of the dominant FCD effect. These temporal features directly reflect the nonlinear coupling between carrier concentration (varying with field intensity squared) and temperature (varying linearly with intensity). The nonlinear dynamics of our system was numerically modeled (Fig. 3d), and become particularly revealing when analyzed in the phase space defined by free carrier density variation  $\Delta N$  and cavity temperature variation  $\Delta T$  (Supplementary

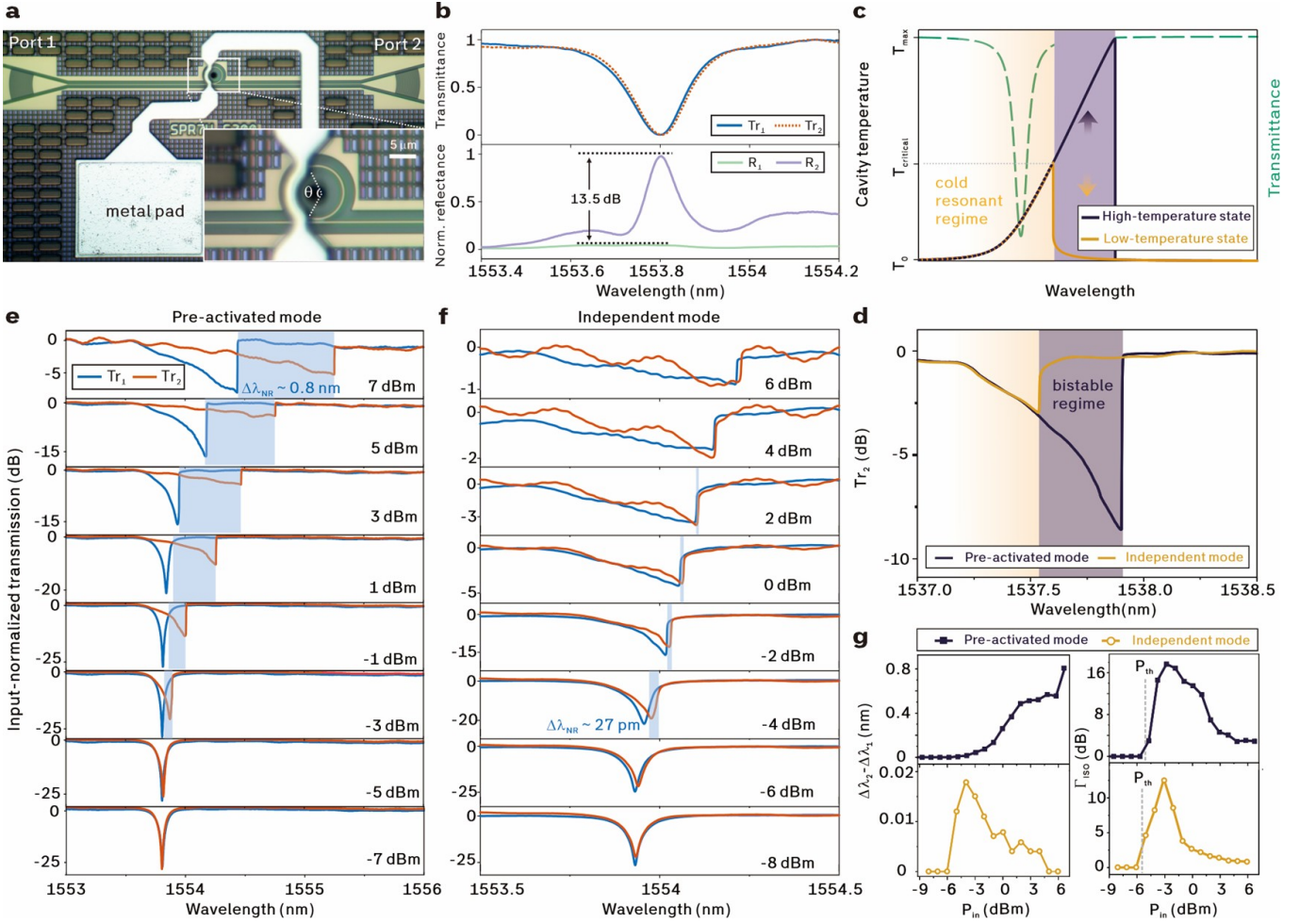


FIG. 2. **Characterization of asymmetric backscattering and non-reciprocal transmission.** **a**, Optical microscope image of a waveguide-coupled spiral ring resonator with radius  $R$  of  $5\ \mu\text{m}$  and  $\theta = 122.4^\circ$ . **b**, Measured transmission spectra  $Tr_1$  and  $Tr_2$  (top) and backreflection spectra  $R_1$  and  $R_2$  (bottom) under bidirectional excitation.  $P_{\text{in}}$  was set to  $-11\ \text{dBm}$ . **c**, Thermal equilibrium diagram illustrating cavity temperature  $T$  versus wavelength for two operational modes. The cold resonant regime and bistable regime are denoted with the orange and purple shaded areas, respectively. **d**, Characterized optical bistability in transmission spectra  $Tr_2$ . **e–f**, Measured transmission spectra  $Tr_1$  and  $Tr_2$  for the pre-activated (**e**) and the independent mode (**f**), with increasing  $P_{\text{in}}$ . The shaded areas represent the nonreciprocal band. **g**, Summarized evolutions of  $\Delta\lambda_{\text{NR}}$  (left) and  $\Gamma_{\text{ISO}}$  (right) as a function of  $P_{\text{in}}$  for two operation modes.  $P_{\text{th}}$  is denoted with gray dashed lines.

Note 7 and Methods). As  $P_{\text{in}}$  surpasses  $P_{\text{SP}}$ , the system undergoes a bifurcation. Beyond this point, the competing FCD and TO effects can no longer maintain equilibrium, instead forming stable limit cycles, demonstrating the characteristic Lyapunov stability of self-sustained oscillations.

Each cycle decomposes into four thermodynamic phases (Fig. 3e): I) a carrier-driven phase where FCA induce rapid resonance blueshift through FCD; II) a thermal accumulation phase dominated by gradual TO-induced redshift; III) a recovery phase as resonance detuning reduces intracavity power; and IV) a relaxation phase suggesting that the cavity cools back toward its initial state. Near threshold, weakened FCD effects blend phases I and II, preventing the system from reaching local equilibrium and producing the observed transient spikes

(Fig. 3c). The direction-dependent dynamics are confirmed by the distinct trajectories of limit cycles as well as the activation temperature,  $T_{\text{SP}2}$  and  $T_{\text{SP}1}$ .

The independent mode reveals equally significant but distinct behavior (Fig. 3f–g). While maintaining the same directional asymmetry in thresholds, the SP band narrows substantially, precisely constrained by the bistable regime boundaries. In the bistable regime (case ii), the threshold temperature  $T_{\text{SP}}$  with strong dependence on the injection direction emerges (Fig. 3e), activating a Hopf bifurcation and guiding the system into limit cycles. Under the same input conditions (e.g., case iii), the absence of cumulative heating prevents approaching  $T_{\text{SP}}$  for sustained oscillations, causing the system to return directly to equilibrium ( $\Delta N \approx \Delta T \approx 0$ ) rather than following cyclic trajectories (Fig. 3h). This

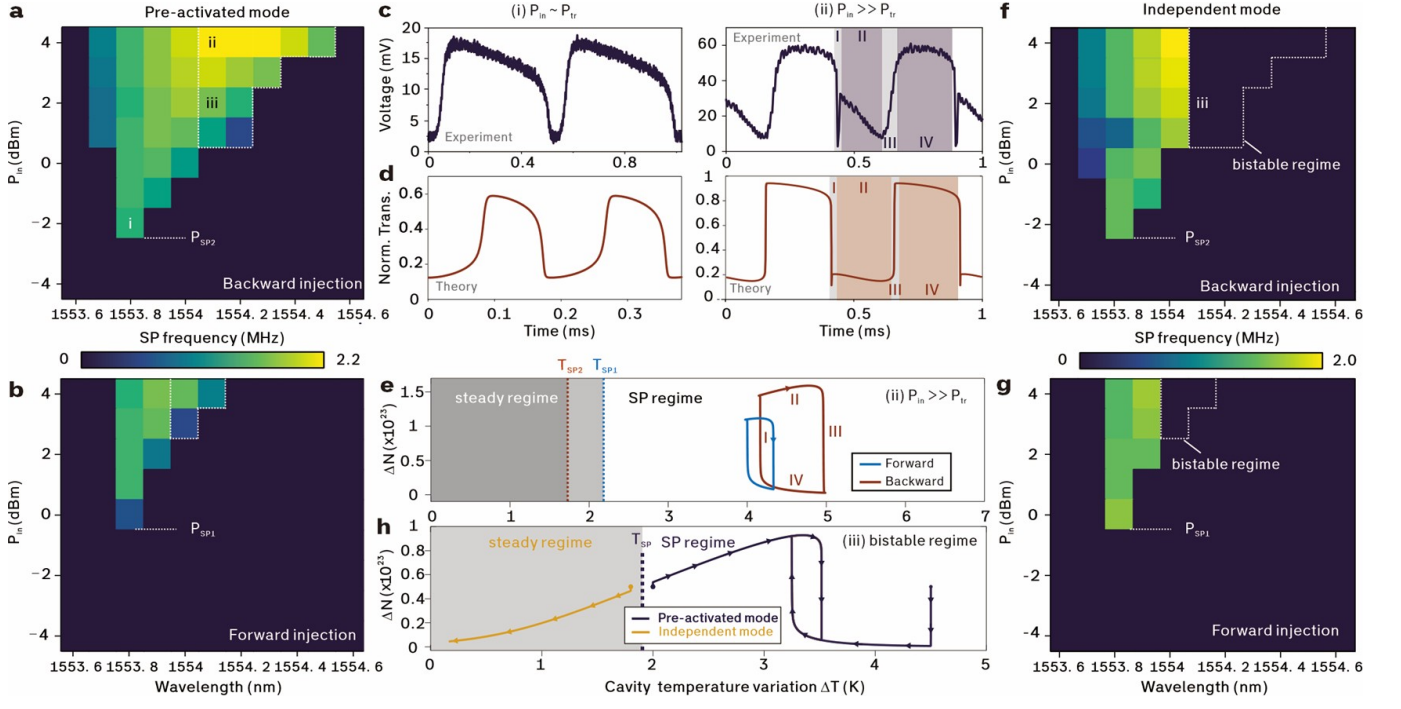


FIG. 3. **Chirality-mediated SP dynamics.** **a–b**, Maps of SP frequency  $\omega_{SP}$  as functions of the probe wavelength  $\lambda_p$  and the input power  $P_{in}$  for backward (a) and forward (b) injection performed in the pre-activated mode. **c**, Measured temporal waveform upon  $P_{in}$  of  $-2$  dBm (top) and  $4$  dBm (bottom) for backward injection. **d**, Modeled temporal responses for (c). **e**, Phase diagram showing the trace of  $\Delta N$ - $\Delta T$  trajectories for two injection directions, with arrows indicating thermodynamic phase progression. **f–g**, Maps of  $\omega_{SP}$  as functions of  $\lambda_p$  and  $P_{in}$  for backward (f) and forward (g) injection performed in the independent mode. **h**, Phase diagram showing the trace of  $\Delta N$ - $\Delta T$  trajectories upon backward injection in both operation modes.

operational-mode dependence provides an additional degree of freedom over SP characteristics in chirality-engineered photonic systems.

## ELECTRICALLY SWITCHABLE PHOTONIC DIODE

The engineered chiral resonance in our photonic diode presents a generic and robust pathway to on-chip nonreciprocity that notably does not require operation at extreme chirality values (i.e.,  $\pm 1$  at EPs). Instead, we achieve full functionality through sign-reversible mode chirality that enables dynamic switching of nonreciprocal transmission direction. In experiments, the electrical reconfiguration of chirality is first characterized in the linear regime (Fig. 4a), where Lorentz reciprocity is well maintained under varying power applied to the phase shifter  $P_{elec}$  (Supplementary Note 8). Measurements of the backreflection spectra  $R_1$  and  $R_2$  reveal a static  $\Delta\Gamma_{BR}$  of  $\sim 0.13$  dB with zero bias, corresponding to a weak chirality of  $\sim -0.007$ . As  $P_{elec}$  increases from 0 to 80 mW, active tuning demonstrates remarkable chirality control (Fig. 4b), spanning from  $\sim -0.17$  (at 40 mW) to  $\sim -0.11$  (at 70 mW), demonstrating in situ control of the diode’s operational state without requiring structural

modifications.

Nonreciprocity in the nonlinear regime was examined upon increased  $P_{elec}$  (Fig. 4c). Under the static condition, a well-defined nonreciprocal window emerges, with  $\Gamma_{ISO}$  of  $\sim 3.6$  dB and a bandwidth of  $\sim 26$  pm, confirming the forward state. At  $P_{elec} = 40$  mW, where chirality reaches an extremum, the optimal performance yields a maximum  $\Gamma_{ISO}$  of  $\sim 10.0$  dB and  $\Delta\lambda_{NR}$  of  $\sim 310$  pm. As  $P_{elec}$  further increases to 70 mW, the system exhibits sign-flipped chirality that inverts the nonreciprocal band with  $\Delta\lambda_{NR}$  of  $\sim 20$  pm, effectively switching the diode to the backward state. Besides, the transition through a near-neutral chirality ( $\sim -0.003$ ) at  $P_{elec} = 20$  mW demonstrates complete nonreciprocity suppression, with residual oscillations showing ultra-narrow linewidth ( $\sim 6$  pm) approaching an ideal disabled state. Fig. 4d presents the evolution of nonreciprocal bandwidth across three characteristic conditions ( $P_{elec}$  of 20, 40, and 70 mW), demonstrating the photonic diode’s reconfigurability between forward, backward, and disabled states.

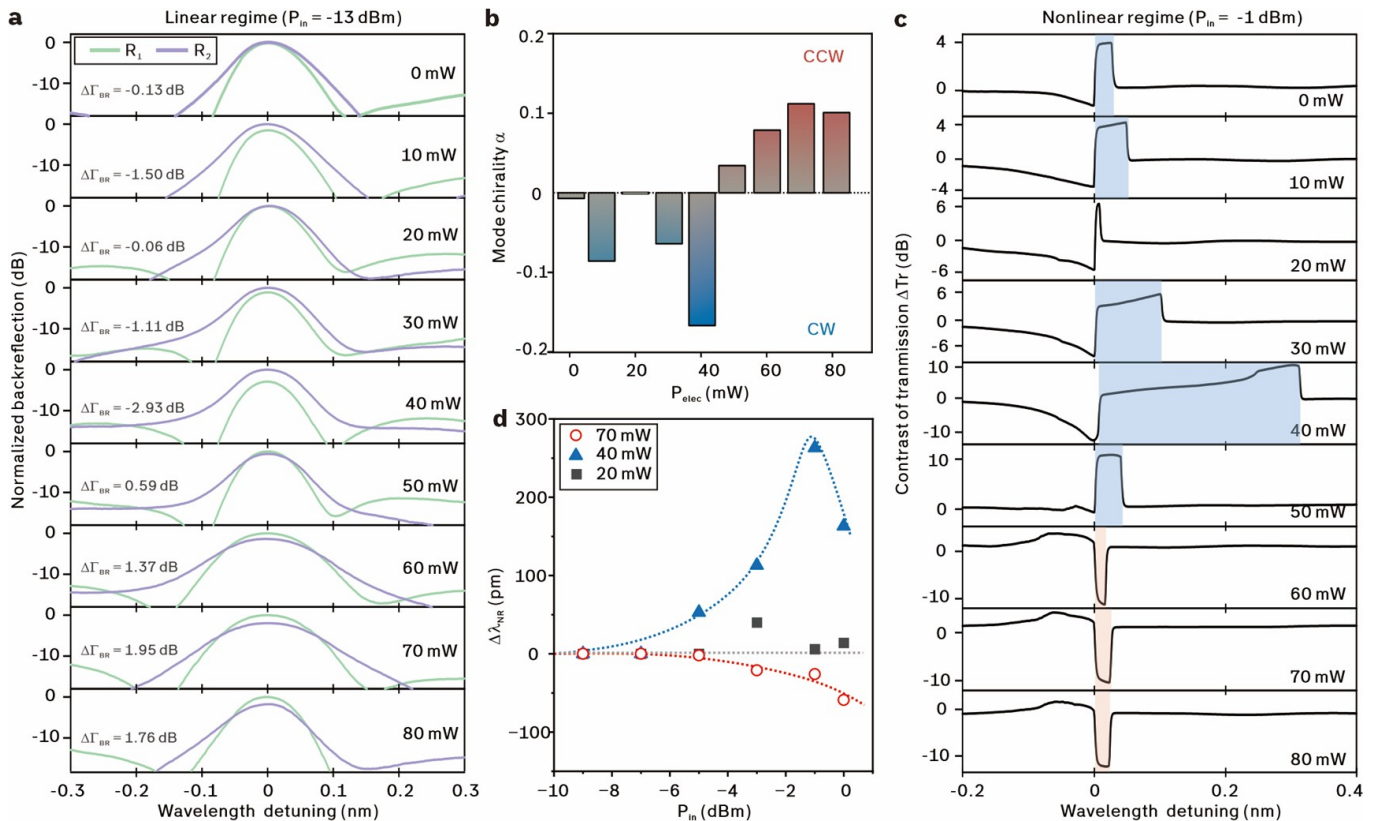


FIG. 4. **Demonstration of an electrically switchable photonic diode.** **a**, Summarized evolution of backreflection spectra  $R_1$  and  $R_2$  upon varying  $P_{\text{elec}}$  from 0 to 80 mW, measured at  $P_{\text{in}} = -13$  dBm. **b**, Extracted mode chirality as a function of  $P_{\text{elec}}$ . **c**, Summarized evolution of  $\Delta Tr$  upon varying  $P_{\text{elec}}$  from 0 mW to 80 mW, measured at  $P_{\text{in}} = -1$  dBm. **d**, Summarized evolution of  $\Delta\lambda_{\text{NR}}$  on the injection power  $P_{\text{in}}$  for three representative  $P_{\text{elec}}$  of 20, 40, and 70 mW.

## DISCUSSION

In summary, we have demonstrated an all-silicon electrically reconfigurable photonic diode based on spiral-shaped microring resonators with engineered chiral resonances. Leveraging the sign-reversible mode chirality, the pronounced intracavity power contrast enables magnetic-free nonreciprocal transmission through asymmetric resonance broadening. Benchmarking against existing on-chip integrated nonlinearity-enabled nonreciprocal devices (Supplementary Note 9), our system features the smallest footprint ( $100 \mu\text{m}^2$ ) while supporting two distinct operational modes, exhibiting a record-high bandwidth of  $\sim 2.9$  nm achieved in the pre-activated mode.

The strong chirality not only enables nonreciprocal transmission but also provides an additional pathway to mediate the direction-dependent SP dynamics. Crucially, electrical reconfiguration of chirality enables dynamic switching between forward, backward, and disabled states. Although fundamentally bound by dynamic reciprocity [21], this electrically-tunable photonic diode represents a critical PIC building block with transformative potential, with engineerable SP dynamics for on-chip all-optical signal processing (e.g., buffer, storage), neuromorphic computing [44], precision metrology [24],

and random number generation. Beyond these immediate applications, the versatility of our approach may unlock unforeseen functionalities in quantum photonics, while its versatility may unlock unforeseen functionalities in quantum photonics [45, 46], particularly for quantum signal processing.

## METHODS

### Modeling

Our analysis employs an effective non-Hermitian Hamiltonian to describe the chiral resonances [23, 47],

$$H = \begin{pmatrix} \Omega & \mathbf{A} \\ \mathbf{B} & \Omega \end{pmatrix}, \quad (1)$$

where the diagonal elements describe the original mode pair, including the energy (real part) and the decay rate (imaginary part), while the off-diagonal elements describe the backscattering of lightwave from CW to CCW ( $\mathbf{A}$ ) and from CCW to CW ( $\mathbf{B}$ ) direction.

The spectral responses can be analyzed via TCMT [48]

$$P_1 = \left| \left( \frac{i\sqrt{\kappa_{\text{in}}}(\omega_c - \Omega)}{(\omega_c - \Omega)^2 - \mathbf{AB}} \right) + \left( \frac{i\sqrt{\kappa_{\text{in}}}\mathbf{B}}{(\omega_c - \Omega)^2 - \mathbf{AB}} \right) \right|^2 |a_{1,\text{in}}|^2, \quad (3)$$

$$P_2 = \left| \left( \frac{i\sqrt{\kappa_{\text{in}}}(\omega_c - \Omega)}{(\omega_c - \Omega)^2 - \mathbf{AB}} \right) + \left( \frac{i\sqrt{\kappa_{\text{in}}}\mathbf{A}}{(\omega_c - \Omega)^2 - \mathbf{AB}} \right) \right|^2 |a_{2,\text{in}}|^2. \quad (4)$$

(see Supplementary Note 1 and 2 for details):

$$i \frac{d}{dt} \begin{bmatrix} \varphi_{\text{CCW}} \\ \varphi_{\text{CW}} \end{bmatrix} = H \begin{bmatrix} \varphi_{\text{CCW}} \\ \varphi_{\text{CW}} \end{bmatrix} + i\sqrt{\kappa_{\text{in}}} \begin{bmatrix} a_{1,\text{in}} \\ a_{2,\text{in}} \end{bmatrix}, \quad (2)$$

where  $\kappa_{\text{in}}$  is the input coupling coefficient, and  $a_{1,\text{in}}$  and  $a_{2,\text{in}}$  are the excitation amplitudes from ports 1 and 2, respectively. Assuming the forward ( $a_{1,\text{in}} = a_{1,\text{in}}e^{-i\omega t}$ ,  $a_2 = 0$ ) and backward ( $a_1 = 0$ ,  $a_{2,\text{in}} = a_{2,\text{in}}e^{-i\omega t}$ ) light injection, the corresponding intracavity power  $P_1$  and  $P_2$  can be expressed as equ.3 and equ.4

For quantifying the nonlinear processes, the rate equations of TPA-induced thermal dynamics and free-carrier dynamics are detailed in Supplementary Note 2. We quantify the absorption power by the contributions based on three components, namely,

$$P_{\text{abs}} = (\gamma_{\text{lin}} + \gamma_{\text{TPA}} + \gamma_{\text{FCA}}) \times U, \quad (5)$$

where  $\gamma_{\text{lin}}$ ,  $\gamma_{\text{TPA}}$  and  $\gamma_{\text{FCA}}$  stand for the linear absorption, TPA- and FCA-induced absorption, respectively,  $U$  is the total intracavity power. The associated TO and FCD effects contributing to resonance detuning are detailed in Supplemental Note 2.

### Device fabrication

Waveguide-coupled spiral ring resonators were fabricated on an SOI platform via a multiple-project wafer (MPW) service (CSiP180A1, CUMEC). The single-mode rib waveguide was designed with a thickness  $T$  of 220 nm and a width  $W$  of 450 nm. Here, by optimizing the gap spacing between the waveguide and the microring to be  $\sim 200$  nm, the microring resonators were designed to work near the critical coupling criteria in the linear regime (i.e., the intrinsic loss coefficient is balanced by the input-coupling coefficient,  $r_{\text{lin}} = \kappa_{\text{in}}$ ). The aluminum-based phase shifter was integrated on the segment between the two spiral edges.

### Device characterization in the linear regime

Transmission spectra were characterized using a wavelength-tunable laser source (TLS570, Santec) at  $\sim 1550$  nm, coupled into a single-mode fiber through free-space optics. Transverse-electric (TE) polarization was ensured using a fiber-based polarization controller

(FPC561, Thorlabs). Waveguide-coupled microring resonators were probed via grating couplers using a dual-fiber configuration, with alignment maintained by a high-precision positioning system featuring active feedback control (AP-SSAS-SIP-SAXYZ, Apico). Transmission signals were measured using a high-speed photodetector (HDETIN08-5G-FC, Lbtek). For characterizing back-reflection signals, fibers with facets polished at a tilted angle of  $8^\circ$  (Corning SMF28e, Photostream Technology) together with a circulator (FCIR-1550-FA, Lbtek) were adopted to suppress background reflections. Spectral acquisition was performed through wavelength scanning with a step resolution of 1 pm.

### Device characterization in the non-linear regime

Characterizations in the nonlinear regime incorporated excitation using an erbium-doped fiber amplifier (GA8129-3314, B&A Technology) with a variable optical attenuator (FVA-3150, EXFO), offering a tunable range of on-chip injection power  $P_{\text{in}}$  between  $-13$  and  $9$  dBm, with the upper limit constrained by the operational range of the variable optical attenuator. Nonreciprocal transmission in the pre-activated mode was characterized by wavelength up-scanning at  $100$  nm/s. For the independent mode, downward scanning at the same rate was performed to ensure acquisition efficiency, given that it results in the same dynamics as stepped scanning. SP waveforms were captured using a high-speed photodetector and a real-time oscilloscope (MHO5104, Rigol). Electrical reconfiguration of the photonic diode was implemented through bias voltage application via probe contacts using a precision source meter (S100, Precise), offering an estimated tuning efficiency of effective refractive index change of  $\sim 2.2 \times 10^{-5}$  RIU/mW.

### ACKNOWLEDGEMENT

We extend our gratitude to Prof. Lorenzo Pavesi and Dr. Stefano Biasi for their fruitful discussions. J.W. acknowledges the support from the National Natural Science Foundation of China under Grants 62422503 and 12474375, the Guangdong Basic and Applied Basic Research Foundation Regional Joint Fund under Grant 2023A1515011944, Science and Technology Innovation Commission of

Shenzhen under Grants JCYJ20220531095604009 and RCYX20221008092907027.

**Notes** The authors declare no competing financial interest.

- 
- \* These authors contributed equally to this work.  
 † [chenyan@nudt.edu.cn](mailto:chenyan@nudt.edu.cn)  
 ‡ [wangjw7@hit.edu.cn](mailto:wangjw7@hit.edu.cn)
- [1] V. S. Asadchy, M. S. Mirmoosa, A. Díaz-Rubio, S. H. Fan, and S. A. Tretyakov, Tutorial on electromagnetic nonreciprocity and its origins, *Proc. IEEE* **108**, 1684 (2020).
  - [2] C. Caloz, A. Alù, S. Tretyakov, D. Sounas, K. Achouri, and Z. L. Deck-Léger, Electromagnetic nonreciprocity, *Phys. Rev. Appl.* **10**, 047001 (2018).
  - [3] Y. Shen, M. Bradford, and J. T. Shen, Single-photon diode by exploiting the photon polarization in a waveguide, *Phys. Rev. Lett.* **107**, 173902 (2011).
  - [4] K. Sato, M. Okano, and Y. Shoji, Ultra-compact microring optical isolator using an aluminum-substituted cobalt ferrite thin film, *Optica* **11**, 889 (2024).
  - [5] L. Bi, J. J. Hu, P. Jiang, D. H. Kim, G. F. Dionne, L. C. Kimerling, and C. A. Ross, On-chip optical isolation in monolithically integrated non-reciprocal optical resonators, *Nat. Photon.* **5**, 758 (2011).
  - [6] S. X. Yuan, L. Chen, Z. W. Wang, W. T. Deng, Z. B. Hou, C. Zhang, Y. Yu, X. J. Wu, and X. L. Zhang, On-chip terahertz isolator with ultrahigh isolation ratios, *Nat. Commun.* **12**, 8 (2021).
  - [7] G. Dushaq, S. Serunjogi, S. R. Tamalampudi, and M. Rasras, Non-reciprocal response in silicon photonic resonators integrated with 2d cucrp2s6 at short-wave infrared, *Light Sci. Appl.* **14**, 157 (2025).
  - [8] X. Guo, Y. Ding, Y. Duan, and X. Ni, Nonreciprocal metasurface with space-time phase modulation, *Light Sci. Appl.* **8**, 123 (2019).
  - [9] D. L. Sounas and A. Alù, Non-reciprocal photonics based on time modulation, *Nat. Photon.* **11**, 774 (2017).
  - [10] N. R. Bernier, L. D. Toth, A. Koottandavida, M. A. Ioannou, D. Malz, A. Nunnenkamp, A. K. Feofanov, and T. J. Kippenberg, Nonreciprocal reconfigurable microwave optomechanical circuit, *Nat. Commun.* **8**, 604 (2017).
  - [11] Z. Shen, Y. L. Zhang, Y. Chen, C. L. Zou, Y. F. Xiao, X. B. Zou, F. W. Sun, G. C. Guo, and C. H. Dong, Experimental realization of optomechanically induced nonreciprocity, *Nat. Photon.* **10**, 657 (2016).
  - [12] E. A. Kittlaus, W. M. Jones, P. T. Rakich, N. T. Otterstrom, R. E. Muller, and M. Rais-Zadeh, Electrically driven acousto-optics and broadband non-reciprocity in silicon photonics, *Nat. Photon.* **15**, 43 (2020).
  - [13] H. Cheng, Y. Zhou, F. Ruesink, M. Pavlovich, S. Gertler, A. L. Starbuck, A. J. Leenheer, A. T. Pomerene, D. C. Trotter, C. Dallo, M. Boady, K. M. Musick, M. Gehl, A. Kodigala, M. Eichenfield, A. L. Lentine, N. T. Otterstrom, and P. T. Rakich, A terahertz-bandwidth non-magnetic isolator, *Nat. Photon.* **19**, 533 (2025).
  - [14] L. Fan, J. Wang, L. T. Varghese, H. Shen, B. Niu, Y. Xuan, A. M. Weiner, and M. Qi, An all-silicon passive optical diode, *Science* **335**, 447 (2012).
  - [15] J. R. Qie, C. Q. Wang, and L. Yang, Chirality induced nonreciprocity in a nonlinear optical microresonator, *Laser Photon. Rev.* **17**, 2200717 (2023).
  - [16] A. Li and W. Bogaerts, Reconfigurable nonlinear non-reciprocal transmission in a silicon photonic integrated circuit, *Optica* **7**, 7 (2020).
  - [17] D. L. Sounas and A. Alù, Nonreciprocity based on nonlinear resonances, *IEEE Antennas Wirel. Propag. Lett.* **17**, 1958 (2018).
  - [18] L. Del Bino, J. M. Silver, M. T. M. Woodley, S. L. Stebbings, X. Zhao, and P. Del’Haye, Microresonator isolators and circulators based on the intrinsic nonreciprocity of the kerr effect, *Optica* **5**, 279 (2018).
  - [19] M. Cotrufo, A. Cordaro, D. L. Sounas, A. Polman, and A. Alù, Passive bias-free non-reciprocal metasurfaces based on thermally nonlinear quasi-bound states in the continuum, *Nat. Photon.* **18**, 81 (2024).
  - [20] M. Cotrufo, S. A. Mann, H. Moussa, and A. Alù, Nonlinearity-induced nonreciprocity-part i, *IEEE Trans. Microw. Theory Tech.* **69**, 3569 (2021).
  - [21] Y. Shi, Z. F. Yu, and S. H. Fan, Limitations of nonlinear optical isolators due to dynamic reciprocity, *Nat. Photon.* **9**, 388 (2015).
  - [22] J. B. Khurgin, Non-reciprocal propagation versus non-reciprocal control, *Nat. Photon.* **14**, 711 (2020).
  - [23] H. Lee, L. Chang, A. Kecebas, D. Mao, Y. Xiao, T. Li, A. Alù, S. K. Özdemir, and T. Gu, Chiral exceptional point enhanced active tuning and nonreciprocity in micro-resonators, *Light Sci. Appl.* **14**, 45 (2025).
  - [24] K. Y. Yang, J. Skarda, M. Cotrufo, A. Dutt, G. H. Ahn, M. Sawaby, D. Vercauteren, A. Arbabian, S. H. Fan, A. Alù, and J. Vuckovic, Inverse-designed non-reciprocal pulse router for chip-based lidar, *Nat. Photon.* **14**, 369 (2020).
  - [25] J. Wang, L. Fan, L. T. Varghese, H. Shen, Y. Xuan, B. Niu, and M. H. Qi, A theoretical model for an optical diode built with nonlinear silicon microrings, *J. Light. Technol.* **31**, 313 (2013).
  - [26] A. D. Li, H. Wei, M. Cotrufo, W. J. Chen, S. Mann, X. Ni, B. C. Xu, J. F. Chen, J. Wang, S. H. Fan, C. W. Qiu, A. Alù, and L. Chen, Exceptional points and non-hermitian photonics at the nanoscale, *Nat. Nanotechnol.* **18**, 706 (2023).
  - [27] B. Peng, S. K. Özdemir, M. Liertzer, W. J. Chen, J. Kramer, H. Yilmaz, J. Wiersig, S. Rotter, and L. Yang, Chiral modes and directional lasing at exceptional points, *Proc. Natl. Acad. Sci. Usa.* **113**, 6845 (2016).
  - [28] L. Tang, J. Tang, W. Zhang, G. Lu, H. Zhang, Y. Zhang, K. Xia, and M. Xiao, On-chip chiral single-photon interface: Isolation and unidirectional emission, *Phys. Rev. A* **99**, 043833 (2019).
  - [29] J. Doppler, A. A. Mailybaev, J. Böhm, U. Kuhl, A. Girschik, F. Libisch, T. J. Milburn, P. Rabl, N. Moiseyev, and S. Rotter, Dynamically encircling an exceptional point for asymmetric mode switching, *Nature* **537**, 76 (2016).
  - [30] S. Soleymani, Q. Zhong, M. Mokim, S. Rotter, R. El-Ganainy, and S. K. Ozdemir, Chiral and degenerate perfect absorption on exceptional surfaces, *Nat. Commun.* **13**, 599 (2022).

- [31] Q. Zhong, A. Hashemi, Ş. K. Özdemir, and R. El-Ganainy, Control of spontaneous emission dynamics in microcavities with chiral exceptional surfaces, *Phys. Rev. Res.* **3**, 013220 (2021).
- [32] L. Fan, L. T. Varghese, J. Wang, Y. Xuan, A. M. Weiner, and M. H. Qi, Silicon optical diode with 40 db nonreciprocal transmission, *Opt. Lett.* **38**, 1259 (2013).
- [33] Y. Yu, Y. H. Chen, H. Hu, W. Q. Xue, K. Yvind, and J. Mork, Nonreciprocal transmission in a nonlinear photonic-crystal fano structure with broken symmetry, *Laser Photon. Rev.* **9**, 241 (2015).
- [34] L. Liu, J. Yue, X. Fan, and W. Xue, On-chip passive optical diode with low-power consumption, *Opt. Express* **26**, 33463 (2018).
- [35] A. M. de las Heras, R. Franchi, S. Biasi, M. Ghulinyan, L. Pavesi, and I. Carusotto, Nonlinearity-induced reciprocity breaking in a single nonmagnetic taiji resonator, *Phys. Rev. Appl.* **15**, 054044 (2021).
- [36] J. W. Li, W. X. Li, Y. Feng, J. Z. Wang, Y. Yao, Y. X. Sun, Y. Zou, J. W. Wang, F. He, J. N. Duan, G. J. Chen, P. P. Shum, and X. C. Xu, On-chip fabrication-tolerant exceptional points based on dual-scatterer engineering, *Nano Lett.* **24**, 3906 (2024).
- [37] H. Lee, A. Kecebas, F. F. Wang, L. Chang, S. K. Özdemir, and T. Y. Gu, Chiral exceptional point and coherent suppression of backscattering in silicon microring with low loss mie scatterer, *Elight* **3**, 20 (2023).
- [38] A. Calabrese, F. Ramiro-Manzano, H. M. Price, S. Biasi, M. Bernard, M. Ghulinyan, I. Carusotto, and L. Pavesi, Unidirectional reflection from an integrated "taiji" microresonator, *Photon. Res.* **8**, 1333 (2020).
- [39] R. Franchi, S. Biasi, D. Piciocchi, and L. Pavesi, The infinity-loop microresonator : A new integrated photonic structure working on an exceptional surface, *APL Photon.* **8**, 056111 (2023).
- [40] Y. H. Chen, J. Li, K. Xu, S. Biasi, R. Franchi, C. R. Huang, J. T. Duan, X. Wang, L. Pavesi, X. C. Xu, and J. W. Wang, Electrically reconfigurable mode chirality in integrated microring resonators, *Laser Photon. Rev.* **18**, 2301289 (2024).
- [41] J. Wiersig, Sensors operating at exceptional points: General theory, *Phys. Rev. A* **93**, 033809 (2016).
- [42] M. A. Miri and A. Alu, Exceptional points in optics and photonics, *Science* **363**, eaar7709 (2019).
- [43] T. J. Johnson, M. Borselli, and O. Painter, Self-induced optical modulation of the transmission through a high-q silicon microdisk resonator, *Opt. Express* **14**, 817 (2006).
- [44] P. Pintus, M. Dumont, V. Shah, T. Murai, Y. Shoji, D. Huang, G. Moody, J. E. Bowers, and N. Youngblood, Integrated non-reciprocal magneto-optics with ultra-high endurance for photonic in-memory computing, *Nat. Photon.* **19**, 54 (2024).
- [45] Z. Zhang, Z. Xu, R. Huang, X. Lu, F. Zhang, D. Li, Ş. K. Özdemir, F. Nori, H. Bao, Y. Xiao, B. Chen, H. Jing, and H. Shen, Chirality-induced quantum non-reciprocity, *Nat. Photon.* **19**, 840 (2025).
- [46] R. Huang, Ş. K. Özdemir, J.-Q. Liao, F. Minganti, L.-M. Kuang, F. Nori, and H. Jing, Exceptional photon blockade: Engineering photon blockade with chiral exceptional points, *Laser Photon. Rev.* **16**, 2100430 (2022).
- [47] J. Wiersig, Structure of whispering-gallery modes in optical microdisks perturbed by nanoparticles, *Phys. Rev. A* **84**, 063828 (2011).
- [48] W. Suh, Z. Wang, and S. H. Fan, Temporal coupled-mode theory and the presence of non-orthogonal modes in lossless multimode cavities, *IEEE J. Quantum Electron.* **40**, 1511 (2004).